Nuclear Science and Techniques (2025) 36:37
https://doi.org/10.1007/s41365-024-01600-4

Comprehensive study of pulse shape discrimination in a Ga-doped zinc oxide scintillating detector

Kuo Zhao[1] · Liang Chen[2] · Ning Lv[1] · Lei-Dang Zhou[3] · Shi-Yi He[2] · Jin-Lu Ruan[2] · Han Wang[1] · Xiao-Ping Ouyang[2]

Received: 12 January 2024 / Revised: 22 July 2024 / Accepted: 27 July 2024 / Published online: 27 January 2025

Abstract

Doping with Ga effectively enhances the crystal quality and optical detection efficiency of zinc oxide (ZnO) single crystals, which has attracted considerable research interest in radiation detection. The application of ZnO:Ga (GZO) in nuclear energy is particularly significant and fascinating at the fundamental level, enabling neutron/gamma discrimination while preserving the response time properties of the single crystal in sub-nanoseconds, maximizing the effective counting rate of the pulsed radiation field. In this study, the single-particle waveform discrimination characteristics of GZO were evaluated for five charged particles (α, β, H^+,Li^+, and O^{8+} and two prevalent uncharged particles (neutrons and gamma rays). Based on the time-correlation single-photon counting (TCSPC) method, the luminescence decay time constants of the charged particles in the GZO crystal were determined as follows: 1.21 ns for H^+, 1.50 ns for Li^+, 1.70 ns for O^{8+}, 1.56 ns for α particles, and 1.09 ns for β particles. Visible differences in the excitation time spectra curves were observed. Using the conventional time-domain or frequency-domain waveform discrimination techniques, waveform discrimination of 14.9 MeV neutrons and secondary gamma rays generated by the CPNG-6 device based on GZO scintillation was successfully implemented. The neutron signal constituted 77.93% of the total, indicating that GZO exhibited superior neutron/gamma discrimination sensitivity compared with that of a commercial stilbene crystal. Using the neutron/gamma screening outcomes, we reconstructed the voltage pulse height, charge height, and neutron multiplication time spectra of the pulsed neutron radiation field. The reconstructed neutron multiplication time spectrum exhibited a deviation of less than 3% relative to the result obtained using a commercial stilbene scintillator. This is the first report in the open literature on the neutron/gamma discrimination and reconstruction of ZnO pulsed radiation-field information.

Keywords Zinc oxide · Scintillation crystal · Pulse shape discrimination · Radiation luminescence · Pulsed neutron radiation field

1 Introduction

Scintillation materials are an important class of energy-conversion materials for a wide range of applications in high-energy physics [1–6], new energy sources [7–12], nuclear medicine [13–18], and geological exploration [19–23]. Although the performance requirements of scintillation materials vary across different application domains, their primary objectives in terms of research and development include high light output, rapid response, and enhanced physicochemical properties. Zinc oxide (ZnO), a wide-bandgap direct-transition semiconductor [24, 25], exhibits excellent scintillation characteristics and radiation resistance [26–28]. In particular, the near-UV exciton-emission

This study was supported by the National Natural Science Foundation of China (Nos. 12205370, 62204198, 12305205, and 12105230) and Young Talents Promotion Program of Shaanxi Provincial Science and Technology Association (No. 20220514).

✉ Kuo Zhao
zhaokuo20240118@163.com

✉ Xiao-Ping Ouyang
ouyangxiaoping@nint.ac.cn

[1] Xi'an Research Institute of Hi-Tech, Xi'an 710025, China

[2] Northwest Institute of Nuclear Technology, Xi'an 710024, China

[3] School of Microelectronics, Xi'an Jiaotong University, Xi'an 710049, China

fluorescence decay lifetime of only a few hundred picoseconds [29–31] endows ZnO with an ultrafast response to high-energy rays and particles (such as X/γ rays [32–37] and α-particles [37–42]), which has been the focus of significant research.

Appropriate doping can mitigate the inherent defects in ZnO materials to a certain extent, enhancing the crystal quality and photoelectric performance [43–46]. Gallium (Ga), as a donor, generates surface donor levels in the lowest region of the conduction band associated with the Fermi surface, resulting in a decrease in the energy gap and enhancement of optical detection efficiency [47–50]. Consequently, ZnO exhibits an ultrafast response time [51–53] and excellent spatial resolution [54, 55] for X-ray detection. Huang et al. [56] employed a raw polycrystalline ZnO material with Ga_2O_3 polycrystalline powder (ratio of 99:1) to synthesize bulk samples via hydrothermal growth. Subsequent cutting and chemical and mechanical polishing treatments produced bulk ZnO:Ga (GZO) single-crystal flakes. Based on the characterization of the fundamental optical properties, we developed an X-ray pinhole imaging system incorporating a GZO single-crystal image converter with nanosecond resolution, thus achieving a spatial resolution of $2.1-2.3\,\mathrm{lp/mm}$ [57]. This method has also been applied in a transient imaging study of the pulsed X-ray radiation field produced by electron emissions from an accelerator diode target [54], and integrated images of the orders of ns and μs were obtained, which laid the foundation for an accurate measurement of weak luminescence and a fast response scintillator in radiation imaging.

In advanced nuclear energy, neutrons emitted by pulsed fusion and fission devices can offer insights into nuclear reactions that occur within the pulse source. Consequently, pulsed neutron detection technology serves as the primary method to investigate the physical dynamics and underlying models associated with the pulsed source [58–63]. Pulsed neutron radiation fields have short durations and significant intensity variations and are frequently accompanied by gamma rays [21, 64, 65]. To accurately reconstruct the original information associated with the radiation field from the measurement results, the detection system must possess both a rapid response time and the ability to discriminate between the waveforms of mixed-field radiation particles [66, 67]. The term pulse shape discrimination (PSD) [68–72] refers to the technique employed to differentiate between the different types of radiation particles based on the premise that distinct radiation particles interact with media according to distinct reaction principles, resulting in a unique time characteristics of the electrical signals generated by the detection system. For instance, at the ISIS Neutron and Muon Source in the UK, approximately half of the neutron instruments employ neutron detectors constructed from ZnS:Ag/^{6}LiF owing to their robust neutron/gamma PSD capabilities [73]. Sykora et al. [74] used ZnO:Zn/^{6}LiF as a substitute for the commercial ZnS:Ag/^{6}LiF to facilitate shorter neutron afterglow. However, the multi-component luminescence process failed to exhibit the sub-nanosecond response time characteristics of ZnO scintillating single crystals. In addition, the fastest response times of existing discrimination detectors, primarily organic scintillators, for neutron/gamma are between 3 ns and 8 ns [69], limiting the neutron count rate within the pulsed radiation field.

Optimizing the pulse radiation-field counting rate while preserving the GZO single-crystal nanosecond response time and achieving neutron/gamma discrimination is challenging. There are few reports on the discrimination of different waveforms using GZO single crystals [75], and the possibility of distinguishing neutron/gamma waveforms remains uncertain. In this study, the single-particle PSD capability of GZO was investigated by addressing the charged-particle waveform discrimination proficiency of GZO and the possibility of mixed-field neutron/gamma discrimination. The potential application of GZO in high-energy nuclear physics and pulse measurement was further explored by processing the neutron/gamma waveform obtained from GZO single-crystal measurements using the classical waveform discrimination algorithm.

2 Pulse shape discrimination of charged particles using a GZO scintillation crystal

2.1 Experimental setup

Neutron production and transport are typically accompanied by gamma rays resulting from the radiation capture effect [21, 46]. Neutrons and gamma rays typically coexist in the form of complex radiation fields. In contrast, isotope radiation sources or heavy-ion accelerators can provide relatively pure charged particles with well-defined energy distributions. We examined the waveform discrimination capabilities of GZO single crystals with respect to various charged particles by analyzing the excitation luminescence response time generated when different types of charged particles irradiate a GZO single crystal.

The dimensions of the GZO single crystal were $30\,\mathrm{mm}\times30\,\mathrm{mm}\times2\,\mathrm{mm}$, fabricated using a hydrothermal technique with a carrier concentration of $1.07\times10^{19}\,\mathrm{cm^{-3}}$ [56]. The luminescence response time was evaluated using the time-correlation single-photon counting (TCSPC) technique [76, 77]. The experimental setup is illustrated in Fig. 1 [78]. The particle emission source was housed in a dark box with the GZO single crystal and a two-way photomultiplier tube (PMT) to prevent the interference of external photons during the single-photon counting

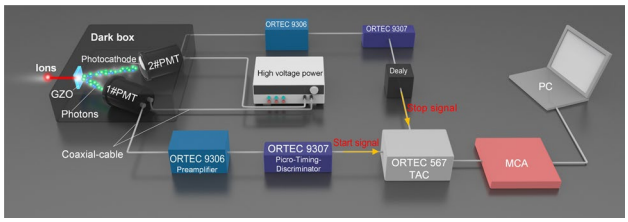

Fig. 1 (Color online) Schematic representation of the experimental layout for the measurement of charged-particle excitation luminescence decay time

method. PMT1#, as shown in Fig. 1, was strategically positioned near the crystal to maximize collection photons as a zero-time signal. Subsequently, PMT2# was moved away from the sample to capture a random single-photon signal. The temporal correlation between the two PMTs signals was then recorded using an electronic acquisition system located behind the PMT. When the energy of the irradiated particle was insufficient, the zero-time signal generated by PMT1# exhibited instability, which could compromise the accuracy of the zero-time signal measurement. Consequently, the TCSPC system was reconfigured into a dual-channel single-photon counting (DCSPC) system to measure the lower-energy charged particles by moving the PMT away from the sample. In this system, an autocorrelation function for the fluorescence time spectrum is represented by the agreement between the signals of the two PMTs, which are both far from the sample. The decay time constant of the sample can be fitted from one branch of the autocorrelation function as a simple exponential function [75]. In the case of the DCSPC, the temporal resolution of the system exceeded 80 ps following calibration using a picosecond light source (EPL-375, Edinburgh; typical pulse width 60 ps).

Five charged-particle sources were used in this experiment: α, β, H^+, Li^+, and O^{8+}. Monoenergetic α particles with energies of 5.48 MeV were generated using an α ^{241}Am radioactive source, whereas β particles with energies ranging from 0 MeV to 1.173 MeV were emitted by a ^{137}Cs radioactive source. Protons (H^+) with energies of 15 MeV, lithium nuclei (Li^+) with energies of 42 MeV, and oxygen nuclei (O^{8+}) with energies of 100 MeV were obtained using the HI-13 tandem accelerator at Chinese Institute of Atomic Energy (CIAE). The ions were guided from the vacuum tube through a 10 μm-thick titanium window in the accelerator tube and impinged on the GZO sample to generate excited luminescence after traversing 5 mm of air. The optical signals were acquired using two microchannel plate PMTs (MCP-PMT, Hamamatsu R3809U).

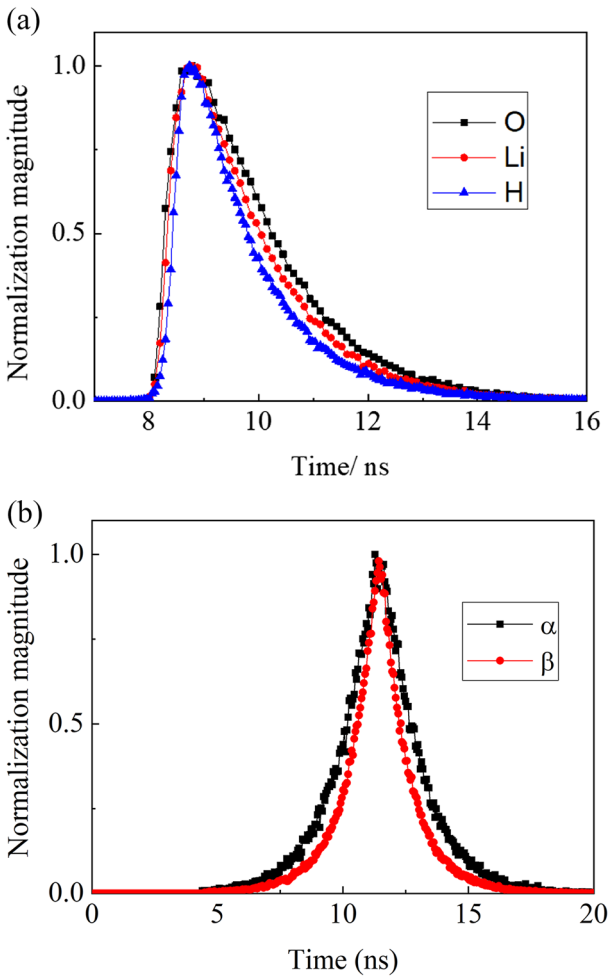

Fig. 2 (Color online) **a** Excitation time spectrum for H^+, Li^+, and O^{8+}. **b** Excitation time spectrum for α and β, where the insert curve is the α particle excited temporal profile obtained using the TCSPC method

2.2 Pulse shape characteristic result

The time-resolved radioluminescence spectra of GZO excited with high-energy H^+, Li^+ and O^{8+}, ions, as measured using the TCSPC method, are presented in Fig. 2a. The corresponding radioluminescence spectra for low-energy α and β particles, obtained using the DCSPC method, are shown in Fig. 2b. A statistical approach to the two channels resulted in the temporal distribution shown in Fig. 2b, which was closer to a Gaussian distribution. The time constants were determined by fitting the data to a single exponential decay function, and the resulting radioluminescence response time constants for the five charged particles are given in Table 1.

Table 1 Decay time constants (τ) obtained from fitting to a single exponential function

Types	Energy (MeV)	τ (ns)
H^+	15	1.21 ± 0.02
Li^+	42	1.50 ± 0.03
O^{8+}	100	1.70 ± 0.04
α	5.48	1.56 ± 0.03
β	0−1.173	1.09 ± 0.02

2.3 Analysis of results

As shown in Fig. 2a, the three types of charged particles generated by the HI-13 tandem accelerator exhibited distinct differences at the trailing edge of the excitation time spectrum, as measured using the TCSPC method. The excitation time spectra of the charged particles generated by the two isotope sources, obtained using the DCSPC method, exhibited an approximately Gaussian distribution. The β-particle time spectrum was characterized by a narrower (or sharper) peak, which significantly contrasted with the broader distribution observed for α particles. The data in Table 1 demonstrated significant differences in the GZO scintillation crystal decay time constants due to the excitation of the five charged particles. The results suggest that the response time of the GZO charged particles to irradiation is contingent on the dE/dx values of the irradiated charged particles. The variation in dE/dx indicates the energy dissipation of charged particles within the unit interval, which corresponds to the ionization potentials of the particles. The β particles exhibited the lowest dE/dx values, whereas the O^{8+} ions exhibited the highest dE/dx values. Although the mass of Li^+ is greater than that of α particles, the energy of Li^+ ions was significantly elevated compared with that of α particles in this experiment, resulting in a lower dE/dx for Li^+ ions relative to α particles. Therefore, the smaller the dE/dx value, the lower the ionization power of charged particles and more rapid the response of the excited GZO scintillation crystal. These findings suggest that GZO can discriminate between different charged particles, and this experimental approach offers a promising method for discriminating between charged particles.

3 Pulse shape discrimination in neutron/gamma mixed field using the GZO scintillation crystal

3.1 Experimental setup

The 600 kV nanosecond-pulse neutron generator (CPNG-6) at the CIAE can operate in the pulsed mode by implementing deuterium ion source cutting [79]. When the deuterium ion beam is accelerated and used to bombard a deuterium/tritium target, neutrons are generated via D-D or D-T nuclear fusion reactions, with a simultaneous neutron/gamma mixed-pulse radiation field. The ion beam cutting device has demonstrated excellent stability in emitting a half-width 5 μs deuterium ion beam at a working frequency of 1 Hz and generating a 5 μs wide pulsed neutron beam according to the principle of nuclear reactions. The radiation field can produce a composite neutron/gamma signal featuring a distinct neutron multiplication time spectrum. Initially, a sequence of mixed neutron/gamma signals was obtained using a scintillator detector, followed by waveform discrimination. Subsequently, based on the post-discrimination neutron signal, the neutron time spectrum of the pulsed neutron radiation field was reconstituted to validate the efficacy of the waveform discrimination.

A schematic of the CPNG-6 experiment based on a pulse mode is presented in Fig. 3. Upon the activation of the ion source chopper, a square wave signal was transmitted to the oscilloscope as an external trigger signal, thus synchronizing with the time base of the oscilloscope. The oscilloscope captured the voltage signals generated in channels 1 and 2 within the −1 to 9 μs time window. The cylindrical scintillation crystal was directly coupled to the PMT and housed within a stainless-steel shielding shell to protect against light and electromagnetic interference. To acquire precise signal details, a HDO8108A oscilloscope (Teledyne LeCroy) with a maximum sampling rate of 10 GHz and a 12-bit bandwidth

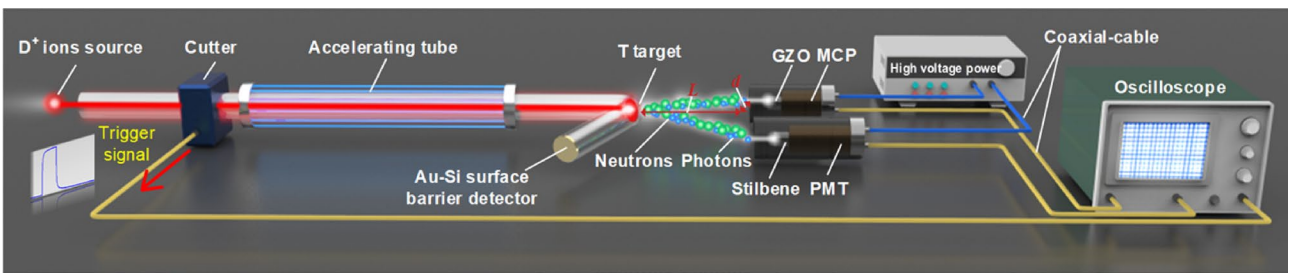

Fig. 3 (Color online) Schematic representation of the layout of the neutron/gamma mixed-field experiment based on the pulsed mode CPNG-6

was employed. The neutron detector and beam channel were situated on the same horizontal plane. To prevent high-flux neutrons in the straight channel from saturating the detector and forfeiting the single-particle waveform signal, the detector was offset from the central axis and target by specific distances, which were strictly recorded. In this experiment, a deuterium ion beam was used to impact a tritium target, generating 14.9 MeV monoenergetic neutrons. A second set of scintillation detectors was constructed on the opposite side of the detector relative to the beam, using a PMT (model ETL-9815) and commercial stilbene crystal (Φ50 mm × 5 mm). A comparative experiment was conducted, and the results of neutron/gamma discrimination and the neutron pulse-time spectra were obtained. To optimize the measurement efficiency, a larger section of the GZO scintillator from the same batch with a diameter of Φ40 mm and thickness of 0.3 mm was employed.

The experimental process and data treatment employed in this study were based on the current-mode counting method [79]. Each neutron/gamma pulse generated a current or voltage signal that was fully captured by a digital oscilloscope. Numerous single-particle signal waveforms were extracted from continuous signals using digital processing methods. The signal analysis extracted critical information, such as the amplitude, the charge value generated by the PMT, type of pulse, and the signal arrival time. The waveforms of typical pulses recorded by the oscilloscope during the experiment after exposing the two types of scintillators to a pulsed radiation field are shown in Fig. 4. The ordinate system was calibrated based on the impedance of the oscilloscope (50 Ω), and the voltage values were converted into current values, facilitating the subsequent calculation of the charge values corresponding to the individual signal waveforms. The initial signals generated by the commercial stilbene scintillator (Φ50 mm × 5 mm) and GZO scintillator (Φ40 mm × 0.3 mm) are shown in Fig. 4a and b, respectively. The dashed black line represents the ion source open signal as the external trigger signal recorded by the pulsed mode oscilloscope. The neutron/gamma signal obtained by the GZO scintillator was faster, but smaller in amplitude. This was owing to the faster response time characteristics and lower irradiated light yield of GZO and the MCP tube.

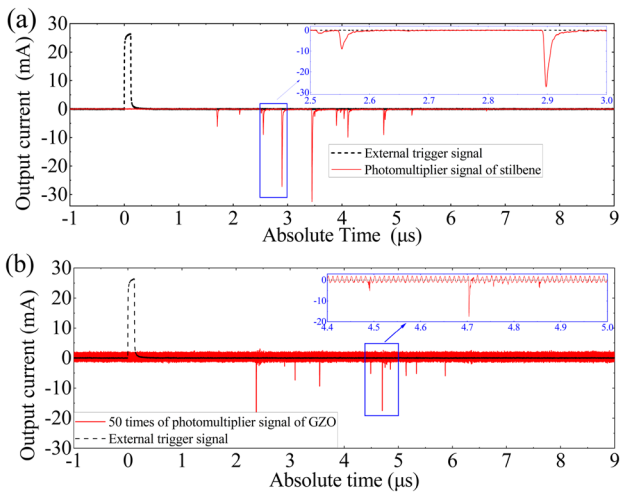

Fig. 4 (Color online) Original waveform generated in **a** the stilbene detector and **b** the GZO crystal

3.2 Pulse shape discrimination results for a single particle

Based on the composite neutron/gamma radiation field generated under the stated experimental conditions, 1800 pulse arrays, each with a duration of 10 μs, were collected. From these, 961 single-particle waveform signals for GZO were extracted, and the lower threshold was set to 5 mV. The most prominent and widely employed time-domain PSD algorithm in the field of neutron/gamma waveform discrimination, referred to as the charge integration method [69, 80], was initially employed to discriminate the pulses associated with the GZO single crystal. In this method, two distinct time intervals were selected to integrate the single-particle signal. Q_{total} was derived by integrating from a fixed time before the peak (denoted by t_{re}, where 're' signifies the 'rise edge') to a specific time following the peak (t_{end}). Q_{slow} was obtained by integrating from t_{re} to a fixed time near the peak (denoted as t_{fe}, where 'fe' signifies the 'falling edge'). Because the neutron pulse drop time was slower than that of gamma, and Q_{slow} constituted a larger portion of Q_{total}, Q_{total}/Q_{slow} was used for neutron/gamma discrimination. The integration intervals of the GZO waveforms in this study were established as −1 to 1 ns (Q_{slow}) and −1 to 12 ns (Q_{total}), respectively, with the peak position designated as the 0 time point. In the case of the commercial stilbene crystal, the integration intervals varied from −10 to 60 ns (Q_{total}), 10 to 60 ns (the difference between (Q_{total}), and 10 to 60 ns and Q_{slow}). The PSD results are shown in Fig. 5.

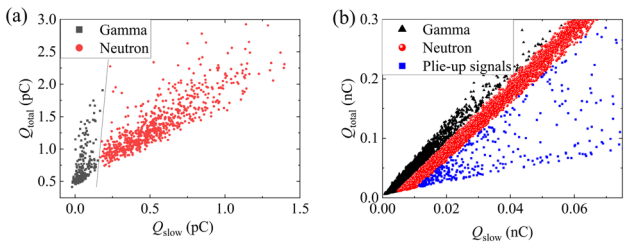

Fig. 5 (Color online) Neutron/gamma discrimination obtained using the charge integration method. **a** GZO (Φ40 mm × 0.3 mm). **b** Commercial stilbene (Φ50 mm × 5 mm)

GZO scintillation demonstrated the ability to distinguish between neutron/gamma single-particle waveforms, which are discernible to the naked eye. Compared with the commercial organic scintillator, the response time for the GZO scintillation single crystals was notably faster, and almost no pulse stacking was observed. However, the detection efficiency was relatively low, resulting in fewer neutron/gamma single-particle signals. After discrimination, the single neutron particle pulses captured by GZO accounted for 77.93% of the total single particles. For the organic scintillator, the neutron contribution was 59.85%, excluding the stacking pulse waveform. The disparate ratios of the neutrons can be attributed to two factors: (i) the disparity in the neutron/gamma detection efficiency of the two types of scintillators and (ii) the varying crystal thickness, where that of the GZO scintillator was thinner than that of stilbene. Consequently, the detection efficiency of gamma rays with a superior penetrating ability was comparatively lower for GZO.

We also applied an established frequency-domain discrimination algorithm [81, 82], the fast Fourier transform (FFT) [83], for pulse discrimination. Typical results derived from the GZO experimental data are shown in Fig. 6. Following normalization, application of FFT, and ordinal summation of the low-frequency components associated with the single-particle pulse, the discrimination coefficient was derived corresponding to the ordinate in Fig. 6a and the abscissa in Fig. 6b. The data presented in Fig. 6a represent 961 individual particle signal pulses, individually plotted as the coordinate coefficients, where neutron/gamma discrimination was executed through the use of the discrimination coefficient size. In Fig. 6b, the discrimination coefficients of the 961 single-particle signals were partitioned into intervals using the operating principle of the multichannel analyzer [46, 84, 85], with the interval counts provided; two near-Gaussian peaks were observed. Utilizing FFT to discriminate the single-particle pulse acquired by GZO enabled an effective neutron/gamma discrimination outcome.

However, the PSD results for the GZO scintillator revealed certain drawbacks compared to the commercial organic scintillator. The edges of the two types of peaks shown in Fig. 6b lacked smoothness, the peaks were asymmetrical, and the relative distance between the peak positions was insufficient. The single-particle neutron waveform utilizing the frequency-domain discrimination algorithm based on FFT accounted for 82.21% of all single particles. This result corresponds to less than a 5% deviation from the classical time-domain algorithm, indicating that the processing outcomes of both algorithms were reliable. These findings suggest that the classical frequency-domain methodology exhibits a degree of applicability in discriminating neutrons/gamma for the GZO scintillation crystal. However, owing to the constraints imposed by the performance of the scintillation crystals, achieving the same level of discrimination as commercial organic scintillators remains a challenge.

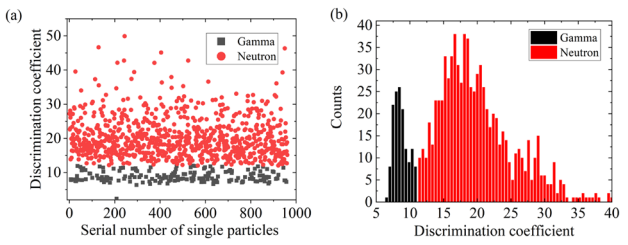

Fig. 6 (Color online) Neutron/gamma discrimination results for GZO obtained via FFT. **a** FFT discriminating coefficients for neutron/gamma distribution. **b** Statistical plot of the neutron/gamma FFT resolution coefficient

3.3 Reconstruction of pulsed neutron radiation-field information based on PSD

C.1. Radiation-field information reconstruction method

The theoretical basis underlying information reconstruction using pulsed radiation-field measurement outcomes has been discussed in detail in a previous publication [79]. The radiation-field reconstruction approach predicated on pulsed-radiation-field measurement results is termed the current-mode counting method. Following neutron/gamma pulse PSD, the digital neutron single-particle waveform was carefully selected from the mixed field. The extraction of multi-dimensional radiation information was performed on each single-particle waveform. Finally, the radiation-field information was reconstructed based on comprehensive multi-particle data. The energy spectrum [86–88] and neutron multiplication time spectrum are the most crucial factors within the radiation-field information associated with pulsed neutrons [89–91].

For radiation fields with long neutron flight distances, the neutron time-of-flight method [92–94] offers an accurate treatment of the energy spectrum. Once a correlation is established between the detector output signal amplitude (or deposited charge) and the neutron energy, the spectrum can be reconstructed using either the neutron pulse-height spectrum (PHS) [40, 47] or charge height spectrum (QHS) [79]. Based on the neutron/gamma discrimination results, the amplitude data of the selected single-particle pulse were systematically enumerated from the minimum to maximum values in accordance with the operational principle of the multichannel analyzer [84, 85]. The number of single particles was determined according to a pre-defined interval of change, enabling the derivation of the neutron PHS. Similarly, the pulse of a single particle (inset of Fig. 4), when integrated along the abscissa, can be used to determine the charge value deposited on the particle detector. A subsequent

application of the multichannel analysis method enabled the derivation of the neutron QHS.

The neutron multiplication time spectrum, also known as the neutron time spectrum, describes the neutron multiplication process as a function of time and can be employed to characterize the nuclear reaction process and total reaction quantity in fusion and fission research [95, 96]. The continuous signal derived from each reaction pulse, as illustrated in Fig. 4, can be used to determine the appearance time of a neutron signal after neutron/gamma discrimination. This information facilitates the extraction of time-related details related to the emergence of a sequence of neutrons during the time spectrum analysis. The window-by-window statistical algorithm (WWS) or time statistics algorithm based on the wavelet packet transform (WPT) [79] can be employed to identify the time at which the neutron signal appears. The neutron time spectrum can then be reconstructed.

C.2. Neutron amplitude spectrum reconstruction results

Employing the discrimination outcomes of the charge integration method illustrated in Fig. 5, 740 neutron signals were extracted from the 961 single-particle pulses. The amplitude of the pulse was directly extracted from the digitally recorded signal using the oscilloscope, followed by an amplitude statistical analysis of the 740 neutron signals. Based on the voltage amplitude of the neutron pulse signal, the PHS was segregated into 50 lanes ranging from low to high, the result of which is shown in Fig. 7a. The solid red squares represent the number of neutrons corresponding to a specific pulse height, as measured by the GZO crystal, after normalization for each reaction pulse. The error bars indicate the uncertainty (68% confidence level) associated with the neutron count in the channel address at this height. The height spectrum resulting from the conversion of the normalized count to logarithmic coordinates is shown in the inset of Fig. 7a. The neutron PHS shown in Fig. 7b was derived from a total of 6453 neutron signals using the commercial stilbene crystal, where the blue data points represent the number of neutrons corresponding to the specific pulse-height channel address normalized for each reaction pulse. The neutron PHS obtained using stilbene was analogously partitioned into 50 channels; the error bars indicate the measurement uncertainty (68% confidence level).

The total deposited charge in the detector corresponding to each neutron single-particle signal was determined by integrating the neutron single-particle pulse signals obtained using GZO and commercial stilbene crystals with respect to time. This process was repeated for 50 channels, generating a neutron QHS for both GZO and commercial stilbene crystals, as illustrated in Fig. 8.

The commercially available stilbene crystal exhibited superior neutron detection efficiency in both the voltage height spectrum and QHS. The neutron detection efficiency of commercial organic scintillators is approximately 8.44×10^{-2} n/pulse, whereas that of the GZO crystal is one order of magnitude lower (8.06×10^{-3} n/pulse). Absolute or relative counts obtained from the statistical analysis reflected the probability distribution of various energy signals generated by the reaction between neutrons and scintillators. The amplitude spectra presented in Figs. 7b and 8b revealed a rectangular distribution for the commercial stilbene system, which became particularly evident as the voltage or charge varied. In addition, a distinct shoulder peak was observed. The experiment employed monoenergetic neutrons with energies of 14.9 MeV generated by D-T fusion, and the amplitude spectrum distribution was in line with the characteristics of the elastic scattering between monoenergetic neutrons and H atoms and the rectangular distribution of the recoil proton energy [96]. The neutron PHS and QHS measured using the GZO crystal exhibited an asymmetric Gaussian distribution characterized by a peak followed by a decline in the e-index without evidence of a flat interval. Transient peaks were observed at 38 mV and 53 mV in the PHS for GZO (Fig. 7a) and at 1.9 pC and 2.2 pC in the QHS (Fig. 8a). We propose that the collisions between 14.9 MeV fast neutrons and ^{16}O nuclei in GZO can result in various responses, including elastic scattering, (n, α), (n, p), (n, d), (n, nα), and (n, np) [95, 97]. The two peaks observed can be attributed to the reactions of (n,α) and (n, nα), whereas the predominant peak in the low-energy region may result from a combination of several factors, including the contribution

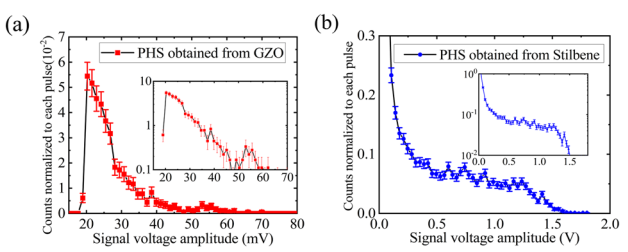

Fig. 7 (Color online) Neutron PHS obtained using GZO and commercial stilbene crystals. **a** PHS obtained with GZO. **b** PHS obtained with stilbene

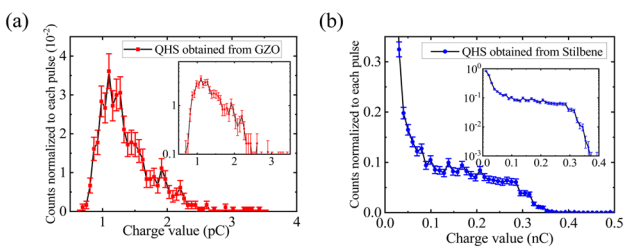

Fig. 8 (Color online) Neutron QHS obtained using GZO and commercial stilbene crystals. **a** QHS obtained using GZO. **b** QHS obtained using stilbene

of low-energy neutrons interacting with material atoms following elastic scattering, inelastic scattering, and reactions involving 14.9 MeV neutrons, as well as the influence of system noise.

The results show that, following neutron/gamma discrimination, the neutron QHS or PHS can be obtained using GZO. The interaction cross section between fast neutrons and ^{16}O is significantly intricate. If the objective is to achieve a comprehensive resolution of the charge amplitude spectrum, or even a reconstruction of the neutron energy spectrum, considerable additional effort will be required. The application of the amplitude spectrum is not further discussed in this paper because the neutron energy spectrum could not be directly obtained from Fig. 7b or Fig. 8b, even for the commercial stilbene crystals.

C.3. Pulsed neutron time spectrum reconstruction results

In this experiment, the distance between the front end of the detector and the target head of the accelerator was $L = 50$ cm (projected length in the north–south direction) and $d = 10$ cm (projected length in the east–west direction). Owing to the short flight distance of neutrons, any broadening of the neutrons in the detector time spectrum caused by the flight time could be ignored and the arrival time of the neutron signal after neutron/gamma discrimination was directly used for neutron time spectrum reconstruction. The WPT [79] was employed to extract the neutron time structure with the CPNG-6 device in pulsed mode, which was recorded using both GZO and the commercial stilbene crystal. For comparison, the results obtained using GZO and the commercial stilbene crystal are shown in Fig. 9. The abscissa represents absolute time. The red time spectrum refers to GZO (with the associated ordinate in red), and the commercial stilbene spectrum is indicated by the dashed blue line (with the associated ordinate in blue). The critical spectral parameters are listed in Table 1. The relative discrepancy between the obtained results and the theoretical

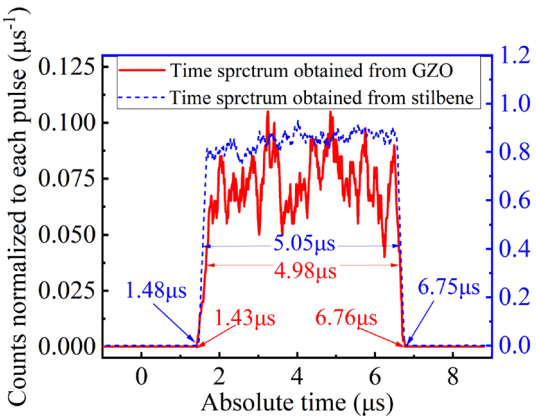

Fig. 9 (Color online) Neutron time spectra obtained using GZO and commercial stilbene crystals

Table 2 Neutron temporal structure parameters obtained from experimental measurements

Scintillator	Base width (μs)	Half width (μs)	Start time (μs)
GZO	5.33(+6.60%)	4.98(−0.40%)	1.43
Stilbene	5.27(+5.40%)	5.05(+1.00%)	1.46
Rel. error	1.14%	1.39%	2.05%

value (5 μs) is indicated in parentheses. Moreover, the comparative errors between the measured outcomes for the two crystals can be assessed using the values in Table 2.

According to the operational principle of the CPNG-6 pulsed neutron source, the predicted neutron burst time spectrum profile for the pulsed radiation field should exhibit a square waveform with a width of 5 μs. The results obtained for GZO and commercial stilbene crystals were essentially in line with the theoretical values. The stilbene measurement revealed a 5.40% deviation from the theoretical value, with a smaller base width value relative to the GZO measurement. The full width at half maximum (FWHM) of the time spectrum for GZO was reduced by 0.4% when compared with the theoretical value, representing an improvement over the stilbene measurement. Considering the neutron burst time point, the relative error for the two crystal results was 2.05%. The detection efficiency of GZO at the neutron burst peak was ca. 0.074 n/μs, which was 11 times smaller than that of the commercial stilbene crystal (0.847 n/μs). The detection efficiency of the commercial stilbene crystals was higher during the interval in which the neutron burst-peak plateau occurred, leading to a smaller statistical uncertainty in the measurement and a smoother plateau curve. Based on the detection efficiency, the number of neutrons collected by GZO was smaller, resulting in a more pronounced waveform oscillation in the plateau curve. However, pulsed neutron radiation fields with a relatively straightforward time structure were detected effectively using a system based on GZO that obtained a pulsed neutron time spectrum by measuring the bottom width or half maximum width of the time spectrum.

4 Conclusion

A comprehensive investigation of the single-particle PSD characteristics of the GZO crystal was conducted for five charged particles (α, β, H^+, Li^+, and O^{8+}) and two prevalent uncharged particles (neutrons and gamma rays). The emission decay time constants of GZO excited by H^+, Li^+, and O^{8+} particles were measured as 1,21 ns, 1.50 ns, and 1.70 ns, respectively, using the TCSPC method. The luminescence decay time constants of GZO excited by α and β particles were measured as 1.56 ns and 1.09 ns,

respectively, using the DCSPC method. The excitation luminescence time spectra of the five particles were also measured. The different excitation time constants enabled GZO to discriminate between the above five charged-particle waveforms. The underlying causes of the disparate responses of the charged particles to GZO require further investigation.

The CPNG-6 device operated in the pulsed mode was employed to generate a pulsed neutron/gamma mixed radiation field. The PSD algorithm in either the time or frequency domains was utilized to distinguish the single-particle signal generated by 14.9 MeV neutrons and secondary gamma rays in the GZO scintillator. This study provides the first reported neutron/gamma discrimination using a ZnO single crystal in a pulsed radiation field. The neutron signal accounted for 77.93% of all single-particle pulses, demonstrating superior neutron/gamma discrimination sensitivity compared with commercial stilbene crystals. The pulsed neutron radiation-field information was reconstructed by utilizing the discriminated neutron signal. This analysis was limited by the absolute light yield of GZO, which exhibited inferior pulsed radiation-field reconstruction effects when compared with commercial scintillators. However, the GZO neutron/gamma discrimination capability enabled the acquisition of the voltage PHS, QHS, and neutron burst time spectrum for pulsed neutron radiation fields using the current-mode counting method. The neutron multiplication time spectrum closely matched that of the commercial scintillator measurements, with a discrepancy of less than 3%. In future research, we plan to use the CSNS [65] to acquire distinct neutron/gamma signals using the time-of-flight method to reconfirm the PSD ability of GZO. As a result, GZO exhibits ultrafast response times and better neutron/gamma discrimination sensitivity and may replace commercial organic scintillators for pulsed neutron source diagnosis with very short durations and high intensities.

The utilization of GZO for the multi-dimensional information processing of a pulsed neutron radiation field reported in this study is the first instance of its application in this domain. Our findings demonstrate the potential of GZO for neutron detection, offering a more responsive scintillator detector variant for the diagnosis of pulsed neutron radiation fields.

Acknowledgements The authors thank Professors Xi-Chao Ruan and Yi-Wen Bao from CIAE for assistance during the experiment on the HI-13 tandem accelerator.

Author contributions All authors contributed to the conception and design of this study. Material preparation, tests, and data collection were performed by Chen Liang, Shi-Yi He, and Jin-Lu Ruan. The experiments were strongly supported by Lei-Dang Zhou and Han Wang. Xiao-Ping Ouyang and Ning Lv supervised this study. The first draft of the manuscript was written by Kuo Zhao, and all authors commented on previous versions of the manuscript. All authors have read and approved the final version of the manuscript.

Data availability The data that support the findings of this study are openly available in Science Data Bank at https://cstr.cn/31253.11.sciencedb.j00186.00399 and https://www.doi.org/10.57760/sciencedb.j00186.00399.

Declarations

Conflict of interest The authors declare that they have no conflict of interest.

References

1. B. Chauhan, B. Dasgupta, V. Datar, A deuterated liquid scintillator for supernova neutrino detection. J. Comol. Astropart. P. **2021**, 005 (2021). https://doi.org/10.1088/1475-7516/2021/11/005
2. K. Fushimi, Y. Kanemitsu, S. Hirata et al., Development of highly radiopure NaI (Tl) scintillator for PICOLON dark matter search project. Prog. Theor. Exp. Phys. **2021**, 043F001 (2021). https://doi.org/10.1093/ptep/ptab020
3. A. Agarwal, H. Budd, J. Capo et al., Total neutron cross-section measurement on CH with a novel 3D-projection scintillator detector. Phys. Lett. B **8**, 29 (2023). https://doi.org/10.3390/psf2023008029
4. Z.Y. Li, Y.M. Zhang, G.F. Cao et al., Event vertex and time reconstruction in large-volume liquid scintillator detectors. Nucl. Sci. Tech. **32**, 49 (2021). https://doi.org/10.1007/s41365-021-00885-z
5. R. Zhang, D.W. Cao, C.W. Loh et al., Using monochromatic light to measure attenuation length of liquid scintillator solvent LAB. Nucl. Sci. Tech. **30**, 30 (2019). https://doi.org/10.1007/s41365-019-0542-1
6. J.N. Dong, Y.L. Zhang, Z.Y. Zhang et al., Position-sensitive plastic scintillator detector with WLS-fiber readout. Nucl. Sci. Tech. **29**, 117 (2018). https://doi.org/10.1007/s41365-018-0449-2
7. R.K. Kothandaraman, Y. Jiang, T. Feurer et al., Near-infrared-transparent perovskite solar cells and perovskite-based tandem photovoltaics. Small Methods. **4**, 2000395 (2020). https://doi.org/10.1002/smtd.202000395
8. M. Liu, G.K. Grandhi, S. Matta et al., Halide perovskite nanocrystal emitters. Adv. Photon. Res. **2**, 2000118 (2021). https://doi.org/10.1002/adpr.202000118
9. H. Esgin, Y. Caglar, M. Caglar, Photovoltaic performance and physical characterization of Cu doped ZnO nanopowders as photoanode for DSSC. J. Alloys Compd. **890**, 161848 (2022). https://doi.org/10.1016/j.jallcom.2021.161848
10. Y. Rong, Y. Hu, A. Mei, H. Tan et al., Challenges for commercializing perovskite solar cells. Science **361**, eaat8235 (2018). https://doi.org/10.1126/science.aat8235
11. L. Zhang, L. Mei, K. Wang et al., Advances in the application of perovskite materials. Nano-Micro Lett. **15**, 177 (2023). https://doi.org/10.1007/s40820-023-01140-3
12. H. Zhu, S. Teale, M.N. Lintangpradipto et al., Long-term operating stability in perovskite photovoltaics. Nat. Rev. Mater. **8**, 569–586 (2023). https://doi.org/10.1038/s41578-023-00582-w
13. D. Kamińska, A. Gajos, E. Czerwiński et al., A feasibility study of ortho-positronium decays measurement with the J-PET scanner based on plastic scintillators. Eur. Phys. J. C **76**, 445 (2016). https://doi.org/10.1140/epjc/s10052-016-4294-3
14. E. Yoshida, F. Obata, K. Kamada et al., Development of cross-hair light sharing PET detector with TOF and DOI capabilities

using fast LGSO scintillator. Phys. Med. Biol. **66**, 225003 (2021). https://doi.org/10.1088/1361-6560/ac2f8b
15. C. Zhang, X. Wang, M. Sun et al., A thick semi-monolithic scintillator detector for clinical PET scanners. Phys. Med. Biol. **66**, 065023 (2021). https://doi.org/10.1088/1361-6560/abe761
16. H. Zhang, H. Tan, W.J. Mao et al., ^{1}8 F-PBR06 PET/CT imaging of inflammation and differentiation of lung cancer in mice. Nucl. Sci. Tech. **30**, 83 (2019). https://doi.org/10.1007/s41365-019-0597-z
17. J.H. Song, J. Zhao, X. Xie et al., Improving the detecting efficiency of suspected gastrointestinal tumors with dual-time-point ^{18} F-FDG PET/CT. Nucl. Sci. Tech. **28**, 138 (2017). https://doi.org/10.1007/s41365-017-0294-8
18. Q.Y. Wei, T.P. Xu, T.T. Dai et al., Development of a compact DOI-TOF detector module for high-performance PET systems. Nucl. Sci. Tech. **28**, 43 (2017). https://doi.org/10.1007/s41365-017-0202-2
19. A. Parshin, V. Morozov, N. Snegirev et al., Advantages of gamma-radiometric and spectrometric low-altitude geophysical surveys by unmanned aerial systems with small scintillation detectors. Appl. Sci. **11**, 2247 (2021). https://doi.org/10.3390/app11052247
20. S. Lv, J. Tang, J. Chen et al., Full-inorganic micro-fiber probe for real-time radiation monitoring. Adv. Mater. Technol. **6**, 2000696 (2021). https://doi.org/10.1016/j.apradiso.2023.110738
21. F. Qiu, F. Zhang, X. Zhang et al., A study on characteristics of background gamma spectrum from $LaCl_3$ detector in pulsed neutron logging. Appl. Radiat. Isot. **195**, 110738 (2023). https://doi.org/10.1016/j.apradiso.2023.110738
22. F. Niu, Z. Liu, D. O'Neil et al., Study of a novel density well-logging tool using A position-sensitive detector. Appl. Radiat. Isotopes. **154**, 108844 (2019). https://doi.org/10.1016/j.apradiso.2019.108844
23. H. Wang, W. Wu, T. Tang et al., A new method for calculating bulk density in pulsed neutron-gamma density logging. Geophysics **85**, D219–D232 (2020). https://doi.org/10.1190/geo2018-0821.1
24. X.Y. Li, J.B. Lu, R.Z. Zheng et al., Comparison of time-related electrical properties of PN junctions and Schottky diodes for ZnO-based betavoltaic batteries. Nucl. Sci. Tech. **31**, 18 (2020). https://doi.org/10.1007/s41365-020-0723-y
25. X.Y. Li, J.B. Lu, Y.M. Liu et al., Exploratory study of betavoltaic battery using ZnO as the energy converting material. Nucl. Sci. Tech. **30**, 60 (2019). https://doi.org/10.1007/s41365-019-0577-3
26. K. Koike, T. Aoki, R. Fujimoto et al., Radiation hardness of single-crystalline zinc oxide films. Phys. Status Solidi C **9**, 1577–1579 (2012). https://doi.org/10.1002/pssc.201100566
27. X. Wen, Q. Zhang, Z. Shao, Magnetron sputtering for ZnO: Ga scintillation film production and its application research status in nuclear detection. Curr. Comput.-Aided Drug Des. **9**, 263 (2019). https://doi.org/10.3390/cryst9050263
28. J.P. Lv, X.J. Li, Defect evolution in ZnO and its effect on radiation tolerance. Phys. Chem. Chem. Phys. **20**, 11882–11887 (2018). https://doi.org/10.1039/c8cp01855c
29. J.T. Jacobsson, S. Viarbitskaya, E. Mukhtar et al., A size dependent discontinuous decay rate for the exciton emission in ZnO quantum dots. Phys. Chem. Phys. **16**, 13849–13857 (2014). https://doi.org/10.3390/nano12142320
30. L. Chen, X.P. Ouyang, Z.B. Zhang et al., Experimental study on scintillation efficiency of ZnO: in to proton response. Chin. Phys. C **35**, 1037 (2011). https://doi.org/10.1088/1674-1137/35/11/011
31. K. Zhang, X.P. Ouyang, Z.H. Song et al., An ideal scintillator-ZnO: Sc for sub-nanosecond pulsed radiation detection. Nucl. Instrum. Meth. A **756**, 14–18 (2014). https://doi.org/10.1016/j.nima.2014.04.044
32. Q. Huang, C. Wang, Q. Shan, Quantitative deviation of nanocrystals using the RIR method in X-ray diffraction (XRD). Nanomaterials **12**, 2320 (2022). https://doi.org/10.3390/nano12142320
33. L. Dejam, S. Kulesza, J. Sabbaghzadeh et al., ZnO, Cu-doped ZnO, Al-doped ZnO and Cu-Al doped ZnO thin films: Advanced micro-morphology, crystalline structures and optical properties. Results Phys. **44**, 106209 (2023). https://doi.org/10.1016/j.rinp.2023.106209
34. M. Kaur, S. Gautam, K.H. Chae et al., Charge transfer and X-ray absorption investigations in aluminium and copper co-doped zinc oxide nanostructure for perovskite solar cell electrodes. Sci. Rep. **13**, 10769 (2023). https://doi.org/10.1038/s41598-023-37754-1
35. W. Lin, D. Chen, J. Zhang et al., Hydrothermal growth of ZnO single crystals with high carrier mobility. Cryst. Growth Des. **9**, 4378–4383 (2009). https://doi.org/10.1021/cg900339u
36. C. Hu, L. Zhang, R.Y. Zhu et al., BaF_2:Y and ZnO: Ga crystal scintillators for GHz hard X-ray imaging. Nucl. Instrum. Meth. A **950**, 162767 (2020). https://doi.org/10.1016/j.nima.2019.162767
37. L. Wang, Y. Xu, X. Cao, J. Huang et al., Diagonal 4-in ZnO nanowire cold cathode flat-panel X-ray source: Preparation and projection imaging properties. IEEE Trans. Nucl. Sci. **68**(3), 338–345 (2021). https://doi.org/10.1109/tns.2021.3051008
38. S.V. Kurudirek, N.E. Hertel, B.D.B. Klein et al., Development of ZnO nanorod-based scintillators grown under a low-temperature hydrothermal method for use in alpha-particle and thermal neutron detectors. IEEE Trans. Nucl. Sci. **63**, 2842–2848 (2016). https://doi.org/10.1109/TNS.2016.2623648
39. J.X. Chen, S.T. Hao, Z.X. Sun et al., Development of the ZnO: Ga nanorod arrays as an alpha particle scintillation screen for the associated particle neutron generator. Appl. Phys. Lett. **120**, 193502 (2022). https://doi.org/10.1063/5.0086133
40. M. Kurudirek, S.V. Kurudirek, N.E. Hertel et al., Vertically well-aligned ZnO nanoscintillator arrays with improved photoluminescence and scintillation properties. Materials **16**, 6717 (2023). https://doi.org/10.3390/ma16206717
41. L.Q. Jing, Z.L. Xu, J. Shang et al., The preparation and characterization of ZnO ultrafine particles. Mater. Sci. Eng. A. **332**, 356–361 (2002). https://doi.org/10.1016/S0921-5093(01)01801-9
42. Y.L. Ma, X.P. Ouyang, J.W. Zhang et al., Properties study of ZnO: Ga crystal on pulsed radiation detections. Chin. Phys. C **34**, 354 (2010). https://doi.org/10.1088/1674-1137/34/3/009
43. M.M. Zeidan, S. Abedrabbo, Enhancing photoluminescence spectra for doped ZnO using neutron irradiation. ACS Omega **8**, 16722–16728 (2023). https://doi.org/10.1021/acsomega.3c00218
44. C.N. Wang, Y.L. Li, F.L. Gong et al., Advances in doped ZnO nanostructures for gas sensor. Chem. Rec. **20**, 1553–1567 (2020). https://doi.org/10.1002/tcr.202000088
45. S. Jian, Z. Tian, J. Hu et al., Enhanced visible light photocatalytic efficiency of La-doped ZnO nanofibers via electrospinning-calcination technology. Adv. Powder Mater. **1**, 100004 (2022). https://doi.org/10.1016/j.apmate.2021.09.004
46. R. He, X.Y. Niu, Y. Wang et al., Advances in nuclear detection and readout techniques. Nucl. Sci. Tech. **34**, 205 (2023). https://doi.org/10.1007/s41365-023-01359-0
47. S. Alamdari, M.S. Ghamsari, M.J. Tafreshi, Novel scintillation properties by entrapping ZnO: Ga nanocrystals in epoxy polymer. Prog. Nucl. Energy **130**, 103495 (2020). https://doi.org/10.1016/j.pnucene.2020.103495
48. W. Mao, M. Jiang, J. Ji et al., Microcrystal modulated exciton-polariton emissions from single ZnO@ ZnO: Ga microwire. Photon. Res. **8**, 175–185 (2020). https://doi.org/10.1364/PRJ.8.000175
49. M. Liu, M. Jiang, Y. Liu et al., Wavelength-tunable green light sources based on ZnO: Ga Nanowire/p-InGaN heterojunctions. ACS Appl. Nano Mater. **4**, 11168–11179 (2021). https://doi.org/10.1021/acsanm.1c02650

50. Y. Liu, R. Dai, M. Jiang et al., Enhanced luminescence/photodetecting bifunctional devices based on ZnO: Ga microwire/p-Si heterojunction by incorporating Ag nanowires. Nanoscale Adv. **3**, 5605–5617 (2021). https://doi.org/10.1002/admt.201800626
51. M.J.F. Empizo, K. Yamanoi, K. Mori et al., Gamma-ray irradiation effects on the optical properties of bulk ZnO single crystals. Appl. Phys. Express **8**, 061101 (2015). https://doi.org/10.7567/apex.8.061101
52. S.Y. He, Y. Li, L. Chen et al., Positive effects of a perovskite film on the radioluminescence properties of a ZnO: Ga crystal scintillator. Materials **15**, 1487 (2022). https://doi.org/10.3390/ma15041487
53. R. Lin, Y. Zhu, L. Chen et al., Ultrafast (600 ps) α-ray scintillators. PhotoniX **3**, 9 (2022). https://doi.org/10.1186/s43074-022-00054-4
54. M. Xu, L. Chen, Z. Yao et al., Transient radiation imaging based on a ZnO: Ga single-crystal image converter. Sci. Rep. **8**, 4178 (2018). https://doi.org/10.1038/s41598-018-22615-z
55. Q. Li, D. Yang, S. Hao et al., Development of the ZnO: Ga microrods-epoxy composite as a scintillation screen for ultrafast X-ray detection. Opt. Mater. **102**, 109805 (2020). https://doi.org/10.1016/j.optmat.2020.109805
56. W. Lin, K. Ding, Z. Lin et al., The growth and investigation on Ga-doped ZnO single crystals with high thermal stability and high carrier mobility. CrystEngComm **13**, 3338–3341 (2011). https://doi.org/10.1039/c1ce05122a
57. M. Xu, L. Chen, B. Liu et al., Effects of photonic crystal structures on the imaging properties of a ZnO: Ga image converter. Opt. Lett. **43**, 5647–5650 (2018). https://doi.org/10.1364/ol.43.005647
58. R. Katano, M. Yamanaka, C.H. Pyeon, Application of linear combination method to pulsed neutron source measurement at Kyoto University Critical Assembly. Nucl. Sci. Eng. **193**, 1394–1402 (2019). https://doi.org/10.1080/00295639.2019.1624084
59. K. Hirota, G. Ichikawa, S. Ieki et al., Neutron lifetime measurement with pulsed cold neutrons. Prog. Theor. Exp. Phys. **2020**, 123C102 (2020). https://doi.org/10.1093/ptep/ptaa169
60. B.A. Turner, K.D. Grange, S.P. Grenley et al., Neutron calorimeter development at fission and fusion pulsed neutron sources. Nucl. Instrum. Meth. A **1052**, 168318 (2023). https://doi.org/10.1016/j.nima.2023.168318
61. L. Ren, Y.C. Han, J.C. Zhang et al., Neutronics analysis of a stacked structure for a subcritical system with LEU solution driven by a D-T neutron source for ^{99} Mo production. Nucl. Sci. Tech. **32**, 123 (2021). https://doi.org/10.1007/s41365-021-00968-x
62. B.L. Li, G.L. Yu, S.F. Shen, Simulation of proton-neutron collisions in inverse kinematics and its possible application. Nucl. Sci. Tech. **32**, 40 (2021). https://doi.org/10.1007/s41365-021-00877-z
63. R.J. Zhu, X. Zhou, Z.H. Liu et al., High-precision and wide-range real-time neutron flux monitor system through multipoint linear calibration. Nucl. Sci. Tech. **31**, 94 (2020). https://doi.org/10.1007/s41365-020-00798-3
64. D. Dong, W. Wu, W. Yue et al., Improving the pulsed neutron-gamma density method with machine learning regression algorithms. J. Petrol. Sci. Eng. **218**, 110962 (2022). https://doi.org/10.1016/j.petrol.2022.110962
65. J.Y. Tang, Q. An, J.B. Bai et al., Back-n white neutron source at CSNS and its applications. Nucl. Sci. Tech. **32**, 11 (2021). https://doi.org/10.1007/s41365-021-00846-6
66. J. Ruan, X. Ouyang, B. Liu et al., Enhanced performance of a pulsed neutron detector by the plastic scintillator with a photonic crystal. Rev. Sci. Instrum. **89**, 123306 (2018). https://doi.org/10.1063/1.5048230
67. K. Zhao, L. Chen, H. Guo et al., Application of stilbene crystals in neutron measurement for monoenergetic neutron beam. J. Instrum. **13**, P10001 (2018). https://doi.org/10.1088/1748-0221/13/10/p10001
68. M.L. Roush, M. Wilson, W.F. Hornyak, Pulse shape discrimination. Nucl. Instrum. Meth. **31**, 112–124 (1964). https://doi.org/10.1016/0029-554x(64)90333-7
69. J. Zhou, A. Abdulaziz, Y. Altmann et al., Generalized method for the optimization of pulse shape discrimination parameters. Nucl. Instrum. Meth. A **1050**, 168184 (2023). https://doi.org/10.1016/j.nima.2023.168184
70. H.R. Liu, Y.X. Cheng, Z. Zuo et al., Discrimination of neutrons and gamma rays in plastic scintillator based on pulse-coupled neural network. Nucl. Sci. Tech. **32**, 82 (2021). https://doi.org/10.1007/s41365-021-00915-w
71. J.X. Li, H.L. Hou, Y.F. Huang et al., Pulse-shaping method for real-time neutron/gamma discrimination at low sampling rates. Nucl. Sci. Tech. **34**, 165 (2023). https://doi.org/10.1007/s41365-023-01306-z
72. J.L. Cai, D.W. Li, P.L. Wang et al., Fast pulse sampling module for real-time neutron-gamma discrimination. Nucl. Sci. Tech. **30**, 84 (2019). https://doi.org/10.1007/s41365-019-0595-1
73. N. Rhodes, E. Schooneveld, R. Eccleston, Current status and future directions of position sensitive neutron detectors at ISIS. Nucl. Instrum. Meth. A **529**, 243–248 (2004). https://doi.org/10.1016/j.nima.2004.04.152
74. G.J. Sykora, E.M. Schooneveld, N.J. Rhodes, ZnO:Zn $/^6$ LiF scintillator–A low afterglow alternative to ZnS:Ag $/^6$ LiF for thermal neutron detection. Nucl. Instrum. Meth. A **883**, 75–82 (2018). https://doi.org/10.1016/j.nima.2017.11.052
75. L. Chen, J. Ruan, M. Xu et al., Comparative study on fluorescence decay time of doped ZnO crystals under α and β excitation. Nucl. Instrum. Meth. A **933**, 71–74 (2019). https://doi.org/10.1016/j.nima.2019.04.095
76. W. Becker, A.W. Castleman, J.P. Toennies et al., *Advanced Time-Correlated Single Photon Counting Techniques* (Springer Science, Business Media, 2005)
77. D. O'Connor, *Time-Correlated Single Photon Counting* (Academic press, 2012)
78. L. Chen, S.Y. He, L.D. Zhou et al., The dependence of fluorescent decay time of ZnO: Ga crystal on instantaneous non-equilibrium carriers induced by charged particles. J. Lumin. **214**, 116520 (2019). https://doi.org/10.1016/j.jlumin.2019.116520
79. K. Zhao, X. Ouyang, H. Guo et al., A transient process observation method based on the non-homogeneous Poisson process model. Chin. Phys. C **45**, 045001 (2021). https://doi.org/10.1088/1674-1137/abde30
80. J. Zhang, M.E. Moore, Z. Wang et al., Study of sampling rate influence on neutron-gamma discrimination with stilbene coupled to a silicon photomultiplier. Appl. Radiat. Isot. **128**, 120–124 (2017). https://doi.org/10.1016/j.apradiso.2017.06.036
81. S. Yousefi, L. Lucchese, M. Aspinall, Digital discrimination of neutrons and gamma-rays in liquid scintillators using wavelets. Nucl. Instrum. Meth. A **598**, 551–555 (2009). https://doi.org/10.1016/j.nima.2008.09.028
82. D.I. Shippen, M.J. Joyce, M.D. Aspinall, A wavelet packet transform inspired method of neutron-gamma discrimination. IEEE Trans. Nucl. Sci. **57**, 2617–2624 (2010). https://doi.org/10.1109/tns.2010.2044190
83. M. Safari, F.A. Davani, H. Afarideh et al., Discrete fourier transform method for discrimination of digital scintillation pulses in mixed neutron-gamma fields. IEEE Trans. Nucl. Sci. **63**, 325–332 (2016). https://doi.org/10.1109/TNS.2016.2514400
84. J. Lewis, J. Warner, C. Einterz et al., Noise reduction in laser photolysis studies of photolabile samples using an optical multichannel analyzer. Rev. Sci. Instrum. **58**, 945–949 (1987). https://doi.org/10.1063/1.1139580

85. T.H. Dinh, T.T. Nguyen, K.H. Nguyen et al., Flexible and low-cost FPGA-based multichannel analyzer for handheld measurement devices. Nucl. Instrum. Meth. A **1018**, 165808 (2021). https://doi.org/10.1016/j.nima.2021.165808
86. G. Wang, L. Zhang, W. Song et al., Optical method based on a gaseous scintillator for neutron energy spectrum measurements. J. Appl. Spectrosc. **87**, 911–918 (2020). https://doi.org/10.1007/s10812-020-01088-x
87. S. Sangaroon, K. Ogawa, M. Isobe et al., Neutron energy spectrum measurement using CLYC7-based compact neutron emission spectrometer in the Large Helical Device. J. Instrum. **16**, C12025 (2021). https://doi.org/10.1088/1748-0221/16/12/c12025
88. J.K. Yang, P.Q. Wang, Z.G. Ren et al., Comparison of neutron energy spectrum unfolding methods and evaluation of rationality criteria. Nucl. Sci. Tech. **33**, 164 (2022). https://doi.org/10.1007/s41365-022-01139-2
89. V. Gribkov, S. Latyshev, R. Miklaszewski et al., A dense plasma focus-based neutron source for a single-shot detection of illicit materials and explosives by a nanosecond neutron pulse. Phys. Scr. **81**, 035502 (2010). https://doi.org/10.1088/0031-8949/81/03/035502
90. E. Grishnyaev, S. Polosatkin, The study of neutron burst shape of a neutron tube driven by dispenser cathode. Nucl. Instrum. Meth. A **828**, 91–96 (2016). https://doi.org/10.1016/j.nima.2016.05.021
91. H. Shishido, H. Yamaguchi, Y. Miki et al., Neutron detection using the superconducting Nb-based current-biased kinetic inductance detector. Supercond. Sci. Technol. **30**, 094003 (2017). https://doi.org/10.1088/1361-6668/aa7a3d
92. D.R. Schaart, Physics and technology of time-of-flight PET detectors. Phys. Med. Biol. **66**, 09TR01 (2021). https://doi.org/10.1088/1361-6560/abee56
93. A.T. Savici, M.A. Gigg, O. Arnold et al., Efficient data reduction for time-of-flight neutron scattering experiments on single crystals. J. Appl. Crystallogr. **55**, 1514–1527 (2022). https://doi.org/10.1107/s1600576722009645
94. B.W. Zheng, W. Zhang, T.Y. Wu et al., Development of real-time double-ring fusion neutron time-of-flight spectrometer system at HL-2M. Nucl. Sci. Tech. **30**, 175 (2019). https://doi.org/10.1007/s41365-019-0702-3
95. M. Carlone, R. Yang, D. Hyde et al., Measurement of neutron yield for a medical linear accelerator below 10 MV. Med. Phys. **50**, 3338–3346 (2023). https://doi.org/10.1002/mp.16416
96. J. Won, J. Song, S. Lee et al., Neutron yield scaling law in laser-cluster fusion experiments. Nucl. Fusion **63**, 066031 (2023). https://doi.org/10.1088/1741-4326/accdea
97. G.F. Knoll, *Radiation Detection and Measurement* (John Wiley & Sons, 2010)